Superfluid 4He as a rigorous test bench for different damping models in nanoelectromechanical resonators

T. Kamppinen ,* J. T. Mäkinen , and V. B. Eltsov
Low Temperature Laboratory, Department of Applied Physics, Aalto University, FI-00076 Aalto, Finland

We have used nanoelectromechanical resonators to probe superfluid 4He at different temperature regimes, spanning over four orders of magnitude in damping. These regimes are characterized by the mechanisms which provide the dominant contributions to damping and the shift of the resonance frequency: tunneling two-level systems at the lowest temperatures, ballistic phonons and rotons at few hundred mK, and laminar drag in the two-fluid regime below the superfluid transition temperature as well as in the normal fluid. Immersing the nanoelectromechanical resonators in fluid increases their effective mass substantially, decreasing their resonance frequency. Dissipationless superflow gives rise to a unique possibility to dramatically change the mechanical resonance frequency *in situ*, allowing rigorous tests on different damping models in mechanical resonators. We apply this method to characterize tunneling two-level system losses and magnetomotive damping in the devices.

I. INTRODUCTION

Nanoelectromechanical (NEMS) resonators have emerged in many fields of physics as ultrasensitive probes of mass and force [1]. For instance, their extreme force resolution enabled measurements sensitive to magnetic field of a single nuclear spin [2]. Recently, detection of a single quantized vortex trapped on a NEMS device in superfluid 4He has been demonstrated [3]. Trapping of a single vortex on a NEMS device in 3He will open new avenues for exciting studies, for example, on Majorana zero modes living in quantized vortex cores [4], the building blocks of a topologically protected quantum computer.

Full understanding of intrinsic device properties and device-fluid interactions is required for detailed analysis of high-precision measurements, e.g., on vortex dynamics, and superfluid 4He is an excellent sandbox for studying those. In this work we provide detailed description of device properties and device-fluid interactions for NEMS resonators of different sizes immersed to the superfluid 4He, and analyze our results using existing theoretical models.

We compare the response of the same devices in vacuum and in superfluid, which provides additional information about the intrinsic device properties. Density of thermal excitations in superfluid 4He becomes vanishingly small at temperatures $T \lesssim 0.2$ K. In absence of quantized vortices, superfluid 4He is practically an ideal fluid with frictionless superflow. The ideal flow of the liquid displaced by the device reduces the resonance frequency via an increase in the effective mass of the resonator, but it does not introduce extra damping. The ability to change both temperature and frequency of a mechanical resonance mode in the same device allows rigorous tests on different damping models. We

apply these tests, in particular, to tunneling two-level systems (TTLS) and magnetomotive damping mechanisms observed in our devices [5]. Beyond nanoelectromechanical resonators, TTLS affect damping, noise, and decoherence in a wide range of quantum-limited measurements [6], for example, in qubits [7] and in optomechanical systems [8]. As the dimensions of those devices are often smaller than the relevant phonon wavelengths, interest in TTLS properties in reduced dimensions extends beyond mechanical resonators [6].

Our experiments reveal how different damping mechanisms scale with mass and frequency. In particular, the damping rate due to magnetomotive damping is found to scale with the resonance frequency f_0 as $\Delta f_m \propto f_0^2 \propto 1/m$ due to increase in the effective mass m of the device. The damping rate resulting from TTLS is found to scale approximately as $\Delta f_{\text{TTLS}} \propto f_0 \propto 1/(mf_0)$ in the low-temperature regime where TTLS relaxation rate is slow compared to the device frequency. Such scaling is not expected from the currently adopted extensions of the standard tunneling model to reduced dimensions [5,6,9] without changes in the coupling between TTLS and phonons, characterized by the parameter γ. We explain the observed scaling with separate coupling parameters γ_1 and γ_2. The parameter γ_1 describes interaction of TTLS with the strain field at the device frequency, and it changes upon immersion of the devices in the fluid. The parameter γ_2 describes TTLS relaxation via a pool of phonons, and is expected to remain unchanged. In our devices γ_1 scales approximately as $\gamma_1 \propto f_0^{-1/2}$. The proposed scalings with mass and frequency can be used as an aid when assessing damping in geometries where current theoretical models are not directly applicable.

A plethora of mechanical devices, including quartz tuning forks [10,11], vibrating wires [12], grids [13], spheres [14], and, recently, microelectromechanical systems (MEMS) and NEMS devices [15–17] have been used to probe the properties of the quantum fluids 3He and 4He. The pursuit for higher
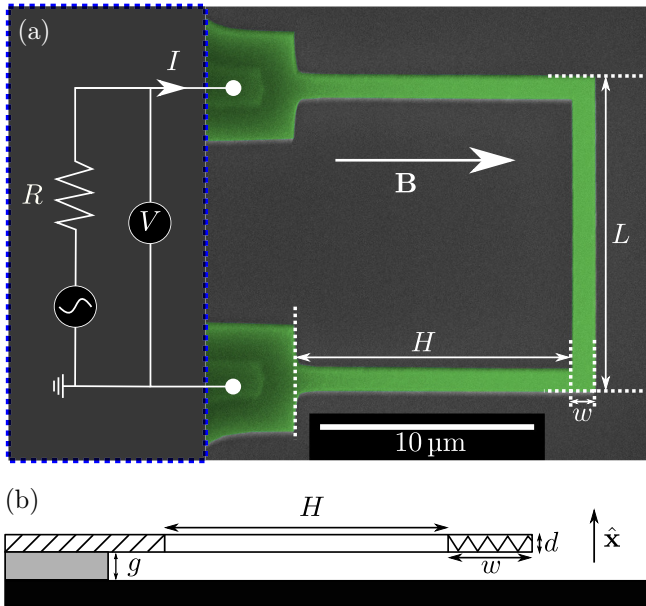
*timo.kamppinen@aalto.fi

FIG. 1. (a) False-color electron micrograph of the sample N1, and outline of the magnetomotive measurement scheme. The device consists of two rectangular legs of length H, and a rectangular paddle of length L connecting the two legs. The legs and paddle comprising of thin beam sections are freestanding after isotropic HF-vapor etch [18]. The wider sections forming the wiring and bonding pads are anchored. (b) Schematic side view of the device of thickness d, with a gap g to the substrate. The motion of the the paddle of width w is directed along $\hat{\mathbf{x}}$. The dimensions (H, L, w, d, and g) for the different devices are tabulated in Table I.

TABLE I. The dimensions of the NEMS devices studied in this work. The dimensions L, H, w are taken from electron micrographs such as shown in Fig. 1. The thickness d is given by quartz crystal microbalance installed in the electron beam evaporator. The tabulated distance g is the nominal thickness of the sacrificial oxide layer (devices N1 and N2) or the nominal thickness of the substrate (devices W1 and W2).

Device	N1	N2	W1	W2
L (µm)	14.7	22.0	60	60
H (µm)	13.0	13.2	44	60
w (µm)	1.1	1.1	20	20
d (nm)	150 ± 8	150 ± 8	200 ± 10	200 ± 10
g (µm)	0.3	0.3	300	300

sensitivity has led to dramatic reduction in the size of the devices, and an increase in the surface-area-to-volume ratio. Thus, the mass enhancement from the fluid is becoming more and more important. We hope that our systematic approach to account for the mass enhancement in the analysis will make comparison of results obtained with different types of devices more straightforward.

Density of thermal excitations in superfluid ^{4}He increases with increasing temperature, and at $T \gtrsim 0.2$ K, momentum exchange with ballistic quasiparticles takes over as the dominant dissipation mechanism in our devices. At $T \gtrsim 0.7$ K, interactions between quasiparticles become important, and viscous drag dominates dissipation. We explain the devices' response using existing models in all the temperature regimes, and achieve good understanding of device-fluid interactions. This is a prequisite for detailed analysis of vortex dynamics in superfluid ^{4}He, and in superfluid ^{3}He where the physics is more involved. Remarkably, the devices are useful thermometers in all the temperature regimes, spanning over four orders of magnitude in dissipation.

II. METHODS

Suspended Π-shaped aluminum NEMS devices have been fabricated. The device geometry is shown in Fig. 1 and the dimensions of the devices are tabulated in Table I. The fabrication process and characterization of the devices in vacuum are described in Refs. [5,18]. NEMS resonators are often located

near surfaces, and it is important to consider whether this proximity influences the operation of the devices in fluids. To test the universality of different damping models, measurements of devices with different aspect ratios and geometries are required. The wide devices W1 and W2 have large aspect ratio $w/d \approx 100$, and are fabricated on an opening in the underlying substrate [5]. The gap below the devices, $g \approx 300$ µm, is determined by the thickness of the substrate. The narrow devices N1 and N2 have aspect ratio $w/d \approx 10$, and are suspended above silicon substrate. For the narrow devices, the gap is ideally determined by the thickness of the sacrificial silicon oxide layer used in the fabrication, $g \approx 0.3$ µm. In practice, the gap is often different due to bending of the devices [18].

Device motion is excited and measured magnetomotively, as shown in Fig. 1. The motion of the device is driven with the Laplace force $F = IL|\mathbf{B}|$, where L is the length of the paddle perpendicular to the magnetic field $\mathbf{B}$, and I is the AC excitation current, produced by an arbitrary waveform generator connected in series with a resistor and the device. The motion of the paddle with velocity $\dot{x}$ induces voltage $V = \dot{x}L|\mathbf{B}|$ which is measured with a lock-in amplifier that is phase locked with the generator. The displacement of the device paddle from the equilibrium position is given by $x(t)$ and the maximum amplitude is x_0. The velocity and displacement amplitude are related via $v_0 = 2\pi f x_0$, where f is the frequency in Hz. We deduce in-phase and quadrature displacement amplitudes x_c and x_s, respectively, from the phase-resolved measurement.

In the harmonic approximation, the resonance frequency of the device is given by

$$f_0 = \frac{1}{2\pi}\sqrt{\frac{k}{m}}, \qquad (1)$$

where the spring constant k and effective mass m are constant. In general, amplitude-dependent deviations in k and m from the low-amplitude values may arise, for instance, due to geometric nonlinearity [19]. The corresponding dynamics equation is

$$m(x)\ddot{x} + 2\pi \Delta f m(x)\dot{x} + k(x)x = F_0 \cos(2\pi f t), \qquad (2)$$

where F_0 is the amplitude of the driving force, Δf is the damping rate of the resonator, and $m(x)$ and $k(x)$ are the generally amplitude-dependent effective mass and spring constant of the resonator. One known model of such nonlinearity is the
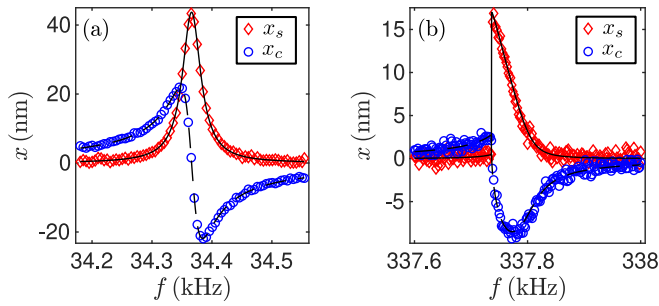
FIG. 2. Example spectra measured in superfluid ^{4}He at $T = 20$ mK. Solid and dashed lines are fits to Eqs. (4) and (5), respectively. (a) Device W1, linear response. We set $D = 0$ in the fitting. (b) Device N1, nonlinear response. Fitting is done with the full equations, giving $D = -0.19$ Hz/nm^2.

Duffing oscillator with the amplitude-dependent resonance frequency [19]

$$f_r = \sqrt{f_0^2 + 2f_0 D x_0^2} \approx f_0 + D x_0^2, \quad (3)$$

where D is to a first approximation a constant. This model was found to describe behavior of our devices well. We fit the NEMS response as a function of frequency to a modified Lorentzian, including the nonlinear frequency shift [19]

$$x_s(f) = \frac{F_0}{m}\left(\frac{1}{2\pi}\right)^2 \frac{(\Delta f)f}{(f_r^2 - f^2)^2 + (\Delta f^2)f^2} \quad (4)$$

and

$$x_c(f) = \frac{F_0}{m}\left(\frac{1}{2\pi}\right)^2 \frac{f_r^2 - f^2}{(f_r^2 - f^2)^2 + (\Delta f^2)f^2}. \quad (5)$$

The wide devices W1 and W2 are always operated in the linear regime, and we set $D = 0$ for them. The narrow devices N1 and N2 become nonlinear at the lowest temperatures in vacuum and in fluid. Example responses and fits are shown in Fig. 2. We extract from the fits the linear resonance frequency f_0 and the damping rate Δf of the mechanical resonators, which give information about dissipative and reactive forces acting on the devices. In the experiments we study how the response is affected by the temperature, magnetic field, and the presence of superfluid ^{4}He.

We restrict this work to the laminar regime, and the drag force is characterized by the term

$$F_d = 2\pi \Delta f m \dot{x} \quad (6)$$

in the dynamics equation (2). The corresponding dissipated power is $P_d = F_d \dot{x}$. Examples of laminar drag forces are viscous drag at low velocities [10], drag due to momentum transfer with ballistic quasiparticles [14], magnetomotive damping [20], and intrinsic TTLS damping in the devices [6]. At high velocities, turbulent drag force proportional to the squared velocity is expected in superfluid ^{4}He [21]. We verify experimentally that we are in the laminar regime by confirming that Δf remains independent of velocity. As the devices are operated at relatively small amplitudes, for which $|f_r - f_0|/f_0 < 10^{-3}$, the effect of nonlinear $m(x)$ to the drag force is assumed to be negligible. However, immersing the devices in a fluid increases the effective mass substantially,

and care has to be taken when converting the parameter Δf obtained from the measurements to drag force or dissipated power. For laminar drag, which is explicitly proportional to the velocity, we have

$$\Delta f \propto 1/m \propto f_0^2 \quad (7)$$

for the same drag force F_d or dissipated power P_d. Quite often, damping is characterized via the inverse quality factor $Q^{-1} = \Delta f/f_0$, which relates the energy lost per cycle to the energy stored in the oscillations. Mass enhancement is expected to increase the quality factor via the additional energy stored in the oscillations. Experimentally, the mass enhancement is determined from the ratio of resonance frequencies in vacuum and in fluid

$$\left(\frac{m_{\text{LHe}}}{m_{\text{vac}}}\right) = \left(\frac{f_{0,\text{vac}}}{f_{0,\text{LHe}}}\right)^2. \quad (8)$$

This relation follows from Eq. (1), assuming k remains constant. In our experiments, a few solid layers of ^{4}He formed on the device surface, when immersed in superfluid ^{4}He, are expected to have negligible contribution to k [22].

The devices are installed in a hermetically sealed container, which is attached to a mixing chamber stage of a dilution refrigerator. The temperature of the mixing chamber stage is monitored with a ruthenium oxide thermometer and controlled with a resistive heater mounted on the mixing chamber plate. The container is connected via a thin capillary to a gas handling system at room temperature. For vacuum measurements, the container is first flushed at room temperature with helium gas, and then pumped with a turbomolecular pump for at least 10 hours before cooling down the cryostat. The container has on its bottom a silver sinter with area $\sim$10 m^2 for thermalizing the fluid. In vacuum measurements, the sinter acts as a cryopump for residual ^{4}He gas. For fluid measurements, helium gas with a nominal purity of 6.0 (impurity content <1 ppm) is admitted to the container slowly via a capillary filling line while the container is kept at a low temperature ($T < 1$ K). This filling procedure is expected to limit amount of remnant vortices in the experimental cell [12].

The samples N1 and N2 were measured at 2.6 bar and the samples W1 and W2 were measured at 3.0 bar fluid pressure, taken at $T = 20$ mK. The volume of fluid in the capillary filling line is negligible compared to the volume in the experimental cell, and while the pressure changes as a function of temperature, fluid density is assumed to be constant. The fluid density and velocity of sound are obtained from Ref. [23], using for the zero-pressure reference density the value given in Ref. [24]. For roton properties, we use results of recent high-resolution neutron scattering experiments [25]. The normal fluid ratio at elevated pressures is obtained by interpolating the tabular data in Refs. [24,26], setting the normal fluid ratio to unity at the lambda-transition temperature. The temperature of the lambda transition at elevated pressures is obtained from Ref. [27]. For the viscosity, we use the values at saturated vapor pressure [24], where we scale the viscosity with the fluid density used in our experiments, and the temperatures with the superfluid transition temperature corresponding to the pressure in the experiment.

III. THEORY

Damping rate of a NEMS device has contributions from different mechanisms, such as tunneling two-level systems damping, magnetomotive damping, damping due to ballistic phonons and rotons, hydrodynamic drag, and possible other contributions, like temperature-independent clamping losses. We assume that the different contributions to the damping rate are additive.

In our experiments, we change the effective mass of the resonator substantially by immersing the device in superfluid ^{4}He. The expected effective mass enhancement in the fluid is [10]

$$\left(\frac{m_{\mathrm{LHe}}}{m_{\mathrm{vac}}}\right) - 1 = \beta \frac{\pi w}{4d} \frac{\rho_{\mathrm{He}}}{\rho_{\mathrm{Al}}} + \frac{BA}{\rho_{\mathrm{Al}} V} \sqrt{\frac{\rho_n \eta}{\pi f_0}}, \quad (9)$$

where $\beta \sim 1$ and $B \sim 1$ are geometrical parameters [28], A and V are the area and volume of the device, ρ_{Al}, ρ_{He}, and ρ_n are the densities of aluminum, the helium fluid, and the normal component of the fluid, and η is the viscosity of the normal fluid component. The first term on the right-hand side of Eq. (9) arises from potential flow of the fluid around the moving body, which couples to the device motion. The last term is due to viscous normal fluid clinging to the motion near the device surface. At low temperatures, $T \lesssim 0.7$ K, density of quasiparticles is low, interquasiparticle interactions leading to viscosity are irrelevant, and the last term can be neglected.

A. Temperature-independent damping

The voltage generated by the motion of the device in a magnetic field drives dissipative currents, which draw power from the device. This results in magnetomotive damping [20]

$$\Delta f_m = a_m B^2, \quad (10)$$

where a_m is a device- and measuring-circuit-dependent parameter and B is the magnetic field strength. In Ref. [5], an analytical expression for a_m relevant to our device geometry is given:

$$a_m = \frac{L^2 d}{3m\rho_e} \left(\frac{w}{H+w}\right)^2, \quad (11)$$

where ρ_e is the electrical resistivity of aluminum at low temperature. At low temperatures, electrical resistivity is independent of temperature, and consequently the magnetomotive damping in our devices is also temperature independent [5]. Equation (11) predicts that magnetomotive damping is independent of frequency, and should scale with the effective mass as $\Delta f_m \propto 1/m$.

In vacuum, the wide devices W1 and W2 demonstrate additional temperature-independent contribution to the damping [5], possibly via acoustic emission to the substrate. When a device is immersed in a fluid, acoustic emission to the fluid is possible as well. A dipole emission model for acoustic emission of NEMS devices is suggested in Ref. [16], resulting in the expression

$$Q_{\mathrm{ac}}^{-1} = \frac{\pi^3}{2} \frac{\rho_{\mathrm{He}}}{\rho_{\mathrm{Al}}} \left(\frac{d_{\mathrm{eff}} f_0}{c_p^2}\right)^2, \quad (12)$$

where $d_{\mathrm{eff}} \approx w$ is the effective beam diameter, and c_p is the speed of sound in the fluid [23]. For our devices, this expression predicts Q_{ac}^{-1} in the range 10^{-5}–10^{-6}, which is negligible compared to other damping mechanisms.

B. TTLS damping

Our devices have been characterized in vacuum before immersing into ^{4}He. It has been found that the main dissipation mechanism at low temperatures is TTLS damping [5]. In the TTLS damping mechanism, the strain caused by the mechanical motion of the device modulates the energy levels of the TTLSs residing in the material of the resonator, leading to an instantaneous population inequilibrium of the TTLSs. The population inequilibrium strives to relax by coupling to the pool of phonon modes in the device. The thermal phonon wavelength is $\lambda_{\mathrm{ph}} = (hc)/(k_B T)$, where $c = \sqrt{E/\rho_{\mathrm{Al}}}$ is the speed of sound in the aluminum beams and E is the Young's modulus. The thermal phonon wavelength exceeds transverse dimensions of NEMS devices at low temperatures, and the dominant contribution to TTLS relaxation often occurs via flexural phonon modes [5,6,9]. In the wider devices W1 and W2, the wavelength λ_{ph} exceeds only the thickness d, making these devices quasi-two-dimendional (quasi-2D) devices. In the narrow devices N1 and N2 the wavelength λ_{ph} exceeds also the beam width w, making them quasi-one-dimensional (quasi-1D) devices.

At low temperatures, TTLS relaxation rate is slow compared to the oscillation frequency of the device, and TTLS damping in 1D devices is given by [5,6]

$$\Delta f_{\mathrm{TTLS,1D}} \approx 0.30 \frac{P_0 \gamma^4}{E^2} \frac{1}{c^{1/2} w d^{3/2}} \frac{(k_B T)^{1/2}}{\hbar^{3/2}}, \quad (13)$$

where P_0 is the TTLS density of states and γ is the coupling between TTLS and phonons. In 2D devices the TTLS damping rate is given by [5,6]

$$\Delta f_{\mathrm{TTLS,2D}} = \frac{\pi}{8\sqrt{3}} \frac{P_0 \gamma^4}{E^2} \frac{1}{cd^2} \frac{k_B T}{\hbar^2}. \quad (14)$$

As the temperature is increased, the TTLS relaxation rate increases, and becomes approximately equal to the resonance frequency at a threshold temperature T^* [29]. Frequency dependence of T^* in different dimensions is discussed in Appendix A. For temperatures above T^*, for all the dimensionalities, TTLS damping saturates to a temperature-independent value [6]

$$\Delta f_{\mathrm{TTLS,HT}} = \frac{\pi f_0}{2} \frac{P_0 \gamma^2}{E}. \quad (15)$$

In experiments, saturation of damping sets in at a temperature T_s, which is expected to be close to the value T^*.

The TTLS contribute to frequency shift of the NEMS devices via relaxation δf_{rel} and resonant δf_{res} absorption mechanisms, and the total frequency shift is a sum of the two effects $\delta f = \delta f_{\mathrm{rel}} + \delta f_{\mathrm{res}}$. The resonant absorption contributes an increase to the resonance frequency of the device [29]

$$\delta f_{\mathrm{res}} = f_0 - f_{0,r} = f_0 \frac{P_0 \gamma^2}{E} \ln\left(\frac{T}{T_r}\right), \quad (16)$$

where $f_{0,r}$ is the resonance frequency taken at the reference temperature T_r. In devices where TTLS damping is governed by coupling to bulk phonons, a decrease in the resonance frequency resulting from relaxation absorption becomes dominant at temperatures $T \gtrsim T^*$, producing a maximum in frequency at approximately T^* [29]. In 1D systems, contribution from the relaxation absorption to the frequency shift is small, and the frequency is expected to increase past T^* [5,9]. To our knowledge, prediction for the frequency shift in the 2D case is not found in the literature. In our NEMS devices, a maximum in frequency is observed at a temperature T_m, which corresponds to a temperature where decrease in frequency from relaxation absorption of 2D or bulk phonons starts dominating over the increase in frequency from the resonant absorption mechanism [5].

C. Damping from ballistic quasiparticle scattering

At low temperatures, the mean-free path of thermal excitations in superfluid ^{4}He is long, and the quasiparticles do not interact with each other at length scales smaller than the characteristic size of the device. Thus, their propagation is ballistic. As a device moves through a superfluid at low temperatures, quasiparticles scatter from its surfaces and exchange momentum with it. The scattering rate of quasiparticles on either side of the moving device is different, and this results in a net drag force acting on the device [14,30,31]. The difference in scattering rates is proportional to the quasiparticle density ρ_q and the volume swept by the device per unit time. The volume is obtained by integrating the device velocity over the area of the device

$$A_p \dot{x} = \int_A \dot{x}(y,z) dy\, dz.$$

Here, $\dot{x}(y,z)$ is the velocity at any point on the device surface, and $\dot{x}$ (without explicit position coordinates) refers to the velocity of the paddle. The average momentum exchanged per quasiparticle is expected to be proportional to the average momentum of the quasiparticles $\langle p_q \rangle = m_q \langle v_q \rangle$, where m_q and $\langle v_q \rangle$ are the mass and average speed of the quasiparticles. We characterize this proportionality with a scattering efficiency Q_q, which is the ratio of momentum exchanged with the device per quasiparticle. In this notation, the drag force resulting from scattering of ballistic quasiparticles is

$$F_d = Q_q A_p \rho_q \langle v_q \rangle \dot{x}, \tag{17}$$

and the corresponding damping rate is

$$\Delta f_q = \frac{Q_q}{2\pi} \frac{A_p}{m} \rho_q \langle v_q \rangle. \tag{18}$$

In the so-called Landau model, the density of phonons is given by [25]

$$\rho_p = \frac{2\pi^2 k_B^4 T^4}{45 c_p^5 \hbar^3} \tag{19}$$

and the same for rotons is

$$\rho_r = \frac{\hbar k_r^4 (m_r)^{1/2}}{3\sqrt{2}\pi^{3/2}(k_B T)^{1/2}} \exp\left(-\frac{\Delta_r}{k_B T}\right), \tag{20}$$

where $k_r(\rho_{He})$ is the roton wave number, $\Delta_r(\rho_{He})$ is the roton gap, and m_r is the effective mass of the roton. The phonon and roton densities obtained from the above expressions agree within 10% with measured densities in Ref. [25] in the regimes where they give the dominant contribution to the damping. For phonons, $\langle v_p \rangle = c_p$, and the damping rate is

$$\Delta f_p = Q_p \frac{A_p}{m} \frac{\pi (k_B T)^4}{45 \hbar^3 c_p^4}. \tag{21}$$

For rotons, $\langle v_r \rangle = \sqrt{2k_B T / \pi m_r}$, and the damping rate is

$$\Delta f_r = Q_r \frac{A_p}{m} \frac{\hbar k_0^4}{6\pi^3} \exp\left(-\frac{\Delta_r}{k_B T}\right). \tag{22}$$

Scattering efficiencies close to unity were found for the microspheres studied in Refs. [14,31]. Deviation from these values in our devices can arise, e.g., due to different shape of the device and different scattering conditions on the device surface (specular or diffuse).

Damping due to ^{3}He impurities in the superfluid ^{4}He can be treated in a similar manner as damping from quasiparticles [32]. The number of ^{3}He atoms per unit volume is small, and Maxwell-Boltzmann statistics with the dispersion relation $\epsilon_3 = p^2/(2m_3)$ and average velocity $v_3 = \sqrt{2k_B T / \pi m_3}$ is assumed. Here, m_3 is the effective mass of ^{3}He particles in superfluid ^{4}He, which is approximately 2.4 times the bare atom mass [33]. The contribution to the damping rate from ^{3}He impurities is

$$\Delta f_3 = Q_3 \frac{1}{2\pi} \frac{A_p}{m} \sqrt{\frac{2k_B T}{\pi m_3}} \rho_3, \tag{23}$$

where ρ_3 is the mass density of ^{3}He atoms. Notably, this contribution has the same functional form on temperature as TTLS damping in 1D devices, Eq. (13). Assuming ^{3}He/^{4}He ratio 1 ppm [34], and $Q_3 = 1$, we find that the damping predicted by Eq. (23) contributes approximately 2% increase in the damping at low temperatures, where the major contribution to the damping is given by Eq. (13).

D. Viscous flow

When the mean-free path of excitations becomes small compared to the device dimensions, viscous effects become important. The viscous penetration depth, expressed here for the normal fluid component, is [35]

$$\delta_n = \sqrt{\frac{2\eta}{\rho_n \omega}}, \tag{24}$$

where η is the dynamic viscosity and ρ_n is the density. For the device frequency $\sim 30\,$kHz, and at temperatures above the λ transition, the viscous penetration depth takes a value $\delta_n \approx 0.5\,\mu$m, which is larger than the device thickness d, but smaller than the device width w. Below the λ-transition temperature the density of the normal fluid component decreases with decreasing temperature and the viscous penetration depth increases. We take the width of the beam w as the characteristic size of the body, as suggested in Ref. [28]. When the characteristic size is large compared to the viscous penetration depth and to the oscillation amplitude, the viscous drag force

TABLE II. The physical properties of the devices studied in this work. The tabulated resonance frequencies f_0 are taken at $T = 20\,\mathrm{mK}$. The parameters Δf_m and Δf_c are the temperature-independent contributions to the damping. The values of the TTLS parameters in vacuum, P_0 and γ, are taken from Ref. [5]. Relative change in TTLS phonon coupling parameter γ_1, photon and roton scattering efficiencies Q_p and Q_r, and the geometrical constant C describing viscous flow are obtained from the fits shown in Fig. 5. The parameters B and β are geometrical parameters describing the mass enhancement resulting from the fluid flow, and are obtained from the fits shown in Fig. 3.

Device	N1	N2	W1	W2
$f_{0,\mathrm{vac}}$ (kHz)	395.2	335.5	73.8	68.0
$f_{0,\mathrm{LHe}}$ (kHz)	337.8	288.9	34.4	31.0
$\Delta f_{m,\mathrm{vac}}$ (Hz)	4 ± 1		124 ± 2	67 ± 2
$\Delta f_{m,\mathrm{LHe}}$ (Hz)	2 ± 3		26.1 ± 0.5	12.8 ± 0.9
$\Delta f_{c,\mathrm{vac}}$ (Hz)			12 ± 3	4 ± 3
$\Delta f_{c,\mathrm{LHe}}$ (Hz)			8 ± 1	4 ± 1
$P_{0,\mathrm{vac}}$ ($10^{-44}\,\mathrm{J}^{-1}\mathrm{m}^{-3}$)	0.49 ± 0.05		7.5 ± 1.3	6.3 ± 1.5
γ_{vac} (eV)	2.9 ± 0.1		0.93 ± 0.04	0.78 ± 0.05
$\gamma_{1,\mathrm{LHe}}/\gamma_{1,\mathrm{vac}}$ [a]	1.20 ± 0.04		1.58 ± 0.28	1.63 ± 0.39
$\gamma_{1,\mathrm{LHe}}/\gamma_{1,\mathrm{vac}}$ [b]	1.06 ± 0.09		1.78 ± 0.39	1.82 ± 0.52
Q_p [Eq. (21)]	2.24 ± 0.25	0.92 ± 0.29	1.66 ± 0.08	1.57 ± 0.10
Q_r [Eq. (22)]	0.64 ± 0.08	0.91 ± 0.05	0.11 ± 0.04	0.20 ± 0.08
C [Eq. (25)]			0.94 ± 0.01	1.05 ± 0.03
B [Eq. (9)]			1.61 ± 0.08	1.64 ± 0.08
β [Eq. (9)]	1.15 ± 0.06	1.1 ± 0.1	0.82 ± 0.04	0.88 ± 0.04

[a]Equations (13) and (14).
[b]Equation (15).

arises mostly from the potential flow of the fluid around the device. The corresponding damping rate is [10]

$$\Delta f_h = \frac{CS}{2m}\sqrt{\frac{\rho_n \eta f_0}{\pi}}, \qquad (25)$$

where C is a numerical constant of the order of unity, and S is the total surface area of the oscillating body.

IV. RESULTS

The response of the devices W1, W2, and N1 has been measured as a function of temperature and magnetic field in vacuum and in superfluid ^{4}He. The device N2 was measured less extensively. Its response was measured at 20 mK in vacuum, and from 20 mK to 0.8 K in superfluid ^{4}He. We start our discussion from the mass enhancement in the fluid and changes in the temperature-independent contributions, as these are used in the subsequent analysis. The following subsections describe the temperature-dependent damping contributions from TTLS, ballistic quasiparticles, and viscous flow. Finally, changes in observed temperature of frequency maxima and temperature of saturation of TTLS damping are discussed. Physical quantities obtained from the fits in the different temperature regimes are tabulated in Table II.

A. Mass enhancement

The temperature dependence of the resonance frequency, and the ratio of effective masses in vacuum and in superfluid ^{4}He for the devices W1, W2, and N1 is shown in Fig. 3. The mass enhancement follows well the theoretical model [Eq. (9)], where at the lowest temperatures the last term involving viscosity can be neglected. For the wide devices W1 and W2, viscous effects are important at $T > 0.8\,\mathrm{K}$. The

geometric constants β and B are tabulated in Table II. We were not able to measure device N1 or N2 at $T > 0.8\,\mathrm{K}$ in superfluid ^{4}He, as the signal amplitude became too small compared to the electrical background. Reliable fitting of the data for the narrow devices N1 and N2 in the viscous regime is not possible due to the limited temperature range. Below 0.8 K, changes in the mass ratio are within a few percent, and for the device N2 mass ratio determined at 20 mK is used for the whole studied temperature range.

B. Temperature-independent damping

The magnetomotive damping is determined by measuring the device damping rate Δf as a function of the magnetic field, and fitting the measured data to Eq. (10), as shown in Fig. 4. The prefactors a_m obtained from the fits for the devices W1, W2, and N1 are tabulated in Table II. The fits show that the magnetomotive damping is independent of frequency, as expected from Eq. (11). The magnetomotive damping is also independent of temperature [5], and is subtracted from the measured damping rates for further analysis.

We fit the damping rate with magnetomotive contribution subtracted, $\Delta f - \Delta f_m$, below the saturation temperature $T < T_s$ to the TTLS model [Eqs. (13) and (14)]. For the narrow device N1, no extra contributions compared to Eq. (13) are found. For the wide devices W1 and W2, an additional temperature-independent contribution Δf_c is included in the fitting. The values Δf_c for the devices W1 and W2 are tabulated in Table II. The damping rates Δf_c are almost the same in vacuum and in fluid, but the corresponding drag force $F_d = 2\pi m \Delta f_c \dot{x}$ and dissipated power $P_d = F_d \dot{x}$ are much higher in the fluid, as the device effective mass is enhanced (see Fig. 3). This is clearly manifested as an offset between the parallel lines in Fig. 4(b), measured at $T = 20\,\mathrm{mK}$, where
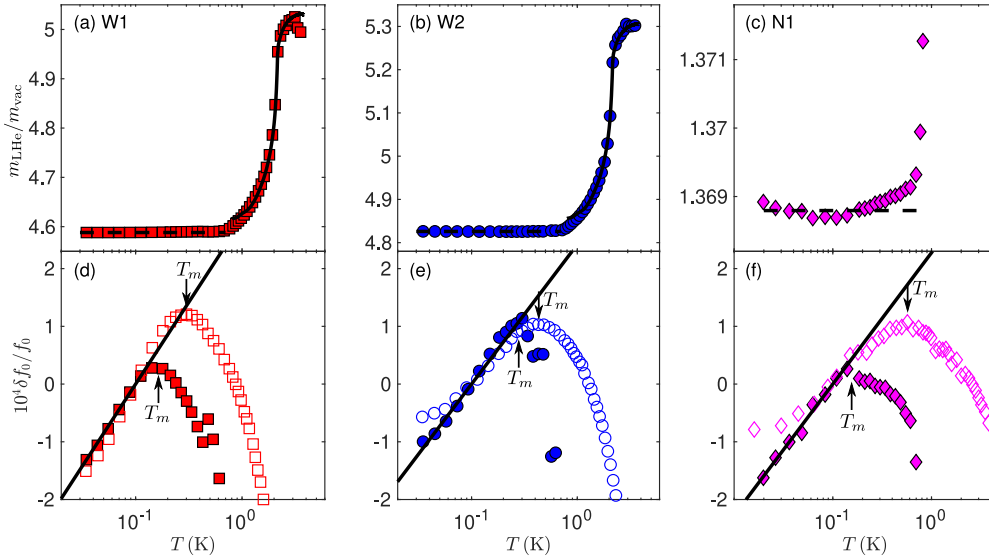
FIG. 3. (a)–(c) Ratio of effective masses in superfluid ^{4}He and vacuum, as a function of temperature. The mass ratio is determined from Eq. (8) using the measured resonance frequencies in vacuum and in fluid. Solid lines are fits to Eq. (9). Viscous effects are negligible at $T \lesssim 0.7$ K. Dashed lines are fits to Eq. (9), neglecting the viscous term. (d)–(f) Detailed view of the resonance frequency shift as a function of temperature, measured in vacuum (empty symbols) and in the fluid (filled symbols). The observed maximum in frequency at temperature T_m is a consequence of combined effect of resonant and relaxation TTLS mechanisms to the frequency shift [5]. Below T_m, the frequency increases logarithmically due to the resonant TTLS mechanism. Lines are fits to Eq. (16). Notably, the slope is practically the same in vacuum and in fluid. Above T_m, the frequency decreases as the frequency shift is dominated by the TTLS relaxation mechanism. In fluid, the resonance frequency is lower, and relaxation process starts dominating at a lower temperature.

temperature-dependent contributions to the damping rate are small.

Acoustic emission to the carrier silicon chip does not seem like a reasonable explanation for the increased dissipated power, as the carrier chip does not support acoustic modes at the frequencies where the wide devices are operated. If the increased dissipation was due to acoustic emission to the fluid, we would expect to see it also in the device N1, according to Eq. (12). In principle, the weak $\Delta f_3 \propto T^{1/2}$ temperature dependence expected from ^{3}He impurities could be mistaken for a temperature-independent contribution. However, at $T < T_s$ damping rate due to ^{3}He impurities $\Delta f_3 \lesssim 0.3$ Hz, obtained from Eq. (23), is small compared to Δf_c.

A possible explanation for the observed temperature-independent contribution is that the entire carrier chip moves due to the elasticity of the glue holding it in place. The resonator exerts a periodic force $F_s = kx$ on its support, which drives the motion of the chip. In fluid, the resonance frequency is lower, and the peak displacement per peak device velocity is higher $[x_0/v_0 = (2\pi f)^{-1}]$. Consequently, the force F_s per unit velocity of the device is higher in the fluid. The oscillations of the chip are expected to be highly damped due to the properties of the glue. For highly overdamped resonator, the amplitude of oscillations is expected to increase towards lower frequencies. Thus, both the force F_s driving the dissipative mechanism and the velocity of the chip and thus the absorbed power are expected to increase when the device is immersed in the fluid. We conclude that oscillations of the carrier chip driven by the device motion can qualitatively explain the observed increase in temperature-independent contribution to the damping in fluid.

C. TTLS regime

The damping rate as a function of temperature in vacuum and in fluid for the devices is shown in Fig. 5. The temperature-independent contributions Δf_m and Δf_c discussed in the previous section, and tabulated in Table II, have been reduced from the data, and the damping rate in the fluid has been scaled with the effective mass m/m_{vac} shown in Fig. 3.

Below 0.2 K, contribution from ballistic quasiparticles to the damping rate is negligible, and damping is governed by the intrinsic TTLS damping mechanism. As seen in Fig. 5, the damping rate has the same functional form in vacuum and in fluid in this temperature regime, i.e., $\Delta f \propto T$ for the wide 2D devices W1 and W2, and $\Delta f \propto T^{1/2}$ for the narrow 1D devices N1 and N2. However, the drag force and the corresponding dissipated power are higher in the fluid, manifested as an offset between the parallel lines in the TTLS regime in Figs. 5(a)–5(c). This corresponds to an increase in the product $P_0 \gamma^4$ in Eqs. (13) and (14). Transition to the saturated damping regime is somewhat masked by the contribution from phonons and rotons in the fluid, but is still visible as a small kink in the data around T_s. Also, the saturated damping regime shows increased dissipation, indicating an increase in the product $P_0 \gamma^2$ in Eq. (15).

We note that the value P_0 describing the TTLS density of states is a property of the TTLS distribution in the material of the device and is not expected to change with immersion of the device into fluid. It is also expected to be energy independent in the relevant range. While a possible energy dependence $P_0 \propto \epsilon^\mu$ in some mesoscopic systems has been suggested, it
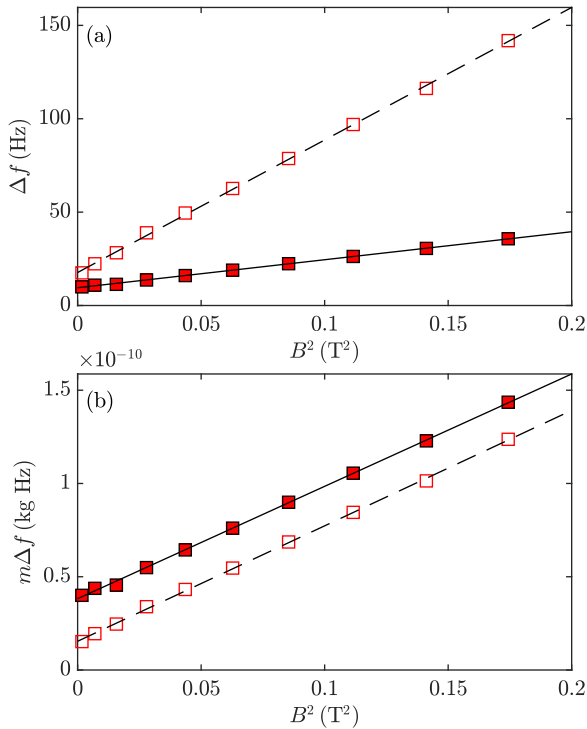
FIG. 4. (a) Magnetic field dependence of the damping rate of the device W1, measured in vacuum (empty symbols) and in superfluid ^{4}He (filled symbols) at $T = 20$ mK. Lines are fits to Eq. (10), including in the fitting an additional constant, which is the field-independent damping rate at that particular temperature. The damping rate decreases in the fluid due to the added mass, as expected from Eq. (7). (b) Magnetic field dependence of the coefficient $m\Delta f$ which is proportional to the drag force in Eq. (6), in vacuum and fluid. The slopes of the fit lines are approximately equal, showing that the drag force resulting from magnetomotive damping is independent of frequency, as expected from Eq. (11).

should manifest as deviations from the observed temperature dependencies of damping, producing $\Delta f_{\text{TTLS,1D}} \propto T^{1/2+\mu}$, $\Delta f_{\text{TTLS,2D}} \propto T^{1+\mu}$, and $\Delta f_{\text{TTLS,HT}} \propto T^{\mu}$ [6]. Our experimental data are best fit with $\mu = 0.0 \pm 0.1$. Thus, we assume that P_0 keeps its vacuum value in the liquid. Another parameter in Eqs. (13) and (14) which potentially changes when the devices are immersed in the liquid is the sound velocity c. We have considered the effect of added mass from the fluid on the phonon dispersion relation in Appendix B, but these corrections have proven to be small.

As a result, we are left with TTLS phonon coupling γ as responsible for the change of the damping in helium. Before further analysis, we note that TTLS interact with phonon modes at very different frequencies: First, the low-frequency mode corresponding to the device oscillations, and, in the case of relaxation absorption, with phonon bath at high frequencies (see Appendix B). In derivation of Eqs. (13)–(16) it is assumed that the coupling γ is the same for all modes. We generalize the approach and allow different couplings: γ_1 for the device-frequency mode and γ_2 for high-frequency modes. Then in Eqs. (13) and (14) γ^4 is replaced by $\gamma_1^2\gamma_2^2$, and in

Eq. (15) γ^2 is replaced by γ_1^2. In vacuum, $\gamma_1 = \gamma_2 = \gamma_{\text{vac}}$. In liquid, we expect γ_2 not to change significantly (see Appendix B and below), and we determine value of γ_1 from the low-temperature behavior of damping, Eqs. (13) and (14), or from the saturated value of damping, Eq. (15), assuming P_0 and γ_2 to keep their values obtained in vacuum. Results are shown in Table II, and both methods give approximately equal values of γ_1 in helium. Remarkably, we empirically find scaling $\gamma_1 \propto f_0^{-1/2}$. Such scaling implies that the inverse quality factor Q^{-1} does not change on immersion of the device to the ideal fluid. This property is verified in Fig. 6.

We note that the frequency shift data shown in Fig. 3 suggest that the product $P_0\gamma^2$ does not change when the devices are immersed in the fluid. Here, the slope of the frequency shift at temperatures $T < T_m$ is proportional to $P_0\gamma^2$ according to Eq. (16). TTLS at energies close to k_BT give the dominant contribution to the frequency shift [29]. Thus, the γ obtained from the frequency shift is relevant for phonons at high thermal frequencies, that is γ_2 in our notation. The frequency data thus support our assumption that γ_2 does not change when the devices are immersed to fluid.

The temperatures T_s (temperature of onset of TTLS damping saturation in Fig. 5) and T_m (temperature of the frequency maxima in Fig. 3), are plotted as a function of the device frequency in Fig. 7. The values of T_s are expected to scale as T^* for the particular device, when the frequency of the device changes. Also, the values T_m are expected to decrease with frequency, but here the distinction between different regimes is not so clear (see Sec. III B). For the 1D device N1, T_s and T_m change more rapidly as a function of frequency than for the 2D devices W1 and W2, as expected for the change in T^* (see Appendix A).

D. Ballistic regime

The roton and phonon scattering efficiencies Q_p and Q_r for the different devices are extracted from the fits shown in Fig. 5, and the values are tabulated in Table II. The phonon scattering efficiency Q_p for the different devices is between 0.9 and 2.2. On average, the values are larger than for spheres oscillating in superfluid ^{4}He, for which Q_p has been found to be close to unity [31]. The difference is perhaps explained by the different geometry of the device (plane versus a sphere), or different scattering conditions (specular or diffuse) on the device surface. For rotons, we find that the scattering efficiency Q_r is smaller than unity for all the devices. Notably, the narrow devices N1 and N2 have substantially larger roton scattering efficiency (0.6–0.9) than the wide devices W1 and W2 (0.1–0.2). The wide devices have large aspect ratio $w/d = 100$ and large gap below the device $g = 300$ μm, while the narrow devices have modest aspect ratio $w/d \approx 7$ and a near surface. While the gap distance determined by the sacrificial oxide layer thickness is $g \sim 0.3$ μm, in practice, the devices often bend due to different thermal expansion coefficients and stress, leading to gap distances $g \sim 1$ μm [18]. The proximity to the surface could affect the damping, e.g., via a squeeze film force, such as observed in gaseous ^{4}He with similar devices in Ref. [18]. On the other hand, with decreasing aspect ratio w/d, scattering from the side walls parallel to the velocity
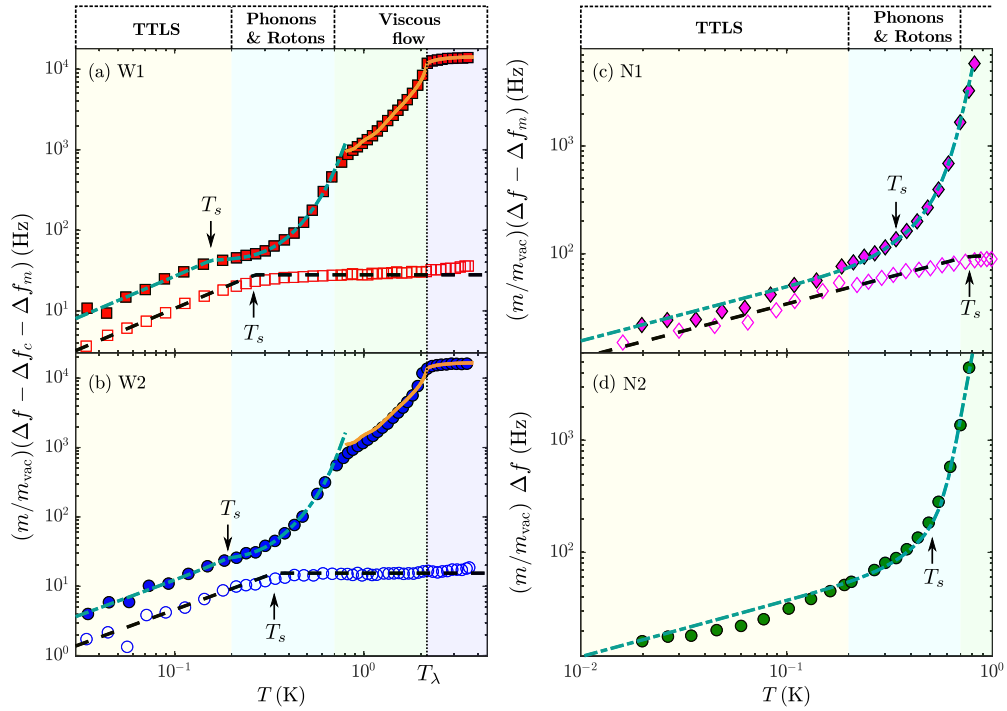
FIG. 5. Damping rate Δf of the devices W1 (a), W2 (b), N1 (c), and N2 (d) as a function of temperature, measured in vacuum (empty symbols), and in superfluid ^{4}He (filled symbols). The damping rate in the fluid is scaled with the ratio of effective masses, with $m = m_{\mathrm{LHe}}$ for the filled symbols and $m = m_{\mathrm{vac}}$ for the empty symbols. Temperature-independent contributions to the damping have been subtracted. The subtracted values are tabulated in Table II, and the missing values are treated as zero. Dashed lines are fits to Eqs. (13)–(15). Dashed-dotted lines are fits to Eqs. (13)–(15), with additional contribution from phonons, Eq. (21), and rotons, Eq. (22), included. The saturation temperature T_s marks the transition from temperature-dependent TTLS damping, governed by Eqs. (13) and (14), to the saturated, temperature-independent, TTLS damping regime governed by Eq. (15). For model lines T_s is used as a fitting parameter. (a), (b) At $T \gtrsim 0.8$ K the damping is governed by viscous flow. Full lines are fits to the viscous drag, Eq. (25), including the constant TTLS contribution at $T > T_s$. The same model works well in fluid and superfluid phases of ^{4}He.

becomes more important, like observed in superfluid ^{3}He for transverse oscillations of a micromechanical plate [17]. Systematic measurements with different gap distances and aspect ratios would be required to reliably distinguish their effect on the scattering efficiencies.

E. Viscous regime

In the viscous regime, above 800 mK, where data on fluid properties are readily available, we fit the device W1 and W2 response to Eqs. (9) and (25), as shown in Figs. 3 and 5. The parameters B, β, and C are tabulated in Table II. The
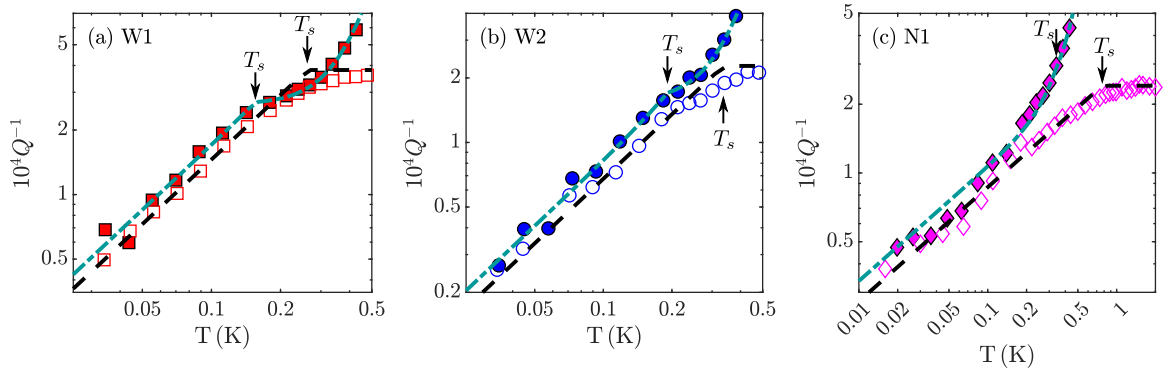

FIG. 6. Inverse quality factor of the devices W1 (a), W2 (b), and N1 (c) in the TTLS damping regime in vacuum (empty symbols) and fluid (filled symbols). Temperature-independent contributions to the damping have been subtracted. Fit lines are the same as in Fig. 5, but scaled with the frequency of the device. At $T \lesssim 0.2$ K, contributions from phonons and rotons are negligible, and the quality factors obtained in vacuum and fluid almost collapse on the same line. Thus, TTLS damping in the low-temperature regime scales approximately as $\Delta f_{\mathrm{TTLS}} \propto f$. At $T \gtrsim 0.2$ K, contribution from phonons starts visibly affecting the device response in the fluid, and the damping increases beyond the intrinsic values.
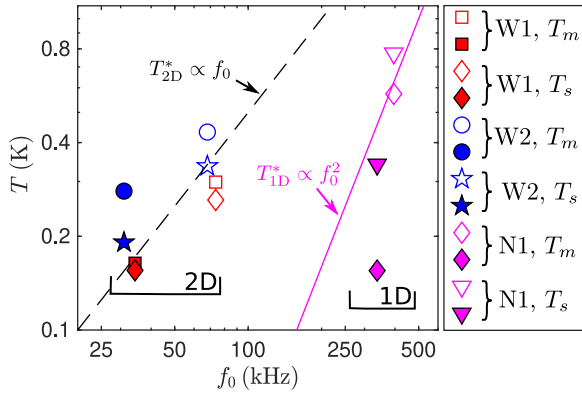
FIG. 7. Temperature of the frequency maximum T_m and saturation temperature of damping T_s as a function of device frequency, extracted from Figs. 3 and 6, respectively. Empty and filled symbols mark data taken in vacuum and fluid, respectively. The saturation damping temperature T_s is expected to scale similarly as the threshold temperature T^*. The lines are guides to the eye, showing the $T^* \propto f_0$ and $T^* \propto f_0^2$ dependencies expected for 2D and 1D devices, respectively (see Appendix A). The change in T_s as a function of frequency for the 1D device N1 is much steeper than for the 2D devices W1 and W2, as expected from the theory. The frequency maximum at T_m is expected to result from relaxation absorption. We observe that T_m scales with the resonance frequency similarly as T_s for the devices W1 and W2. For the device N1, the measured T_m changes more rapidly with frequency than observed T_s and predicted T^*.

parameter C for both devices is very close to unity, and perhaps similar devices could be used for thermometry or viscometry in a fluid even without free parameters. It is also notable that the variation of the parameters B and β between the devices is small, so the frequency could be used as an alternative measuring technique, perhaps without free parameters.

V. CONCLUSIONS

We have measured the damping and frequency shift of NEMS resonators in vacuum and in superfluid ^{4}He at temperatures from 20 mK to 4 K. Our measurements span over four orders of magnitude in damping, enabling rigorous test on the existing models describing device-intrinsic damping and device-fluid interactions.

The dominant device-intrinsic damping mechanism in our devices is TTLS damping. Beyond nanoelectromechanical resonators, TTLS affect noise, dissipation, and decoherence in a wide range of quantum-limited measurements, e.g., in qubits and optomechanical systems. Immersing mechanical resonators in superfluid ^{4}He gave us the possibility to study TTLS damping in a setting, where the frequency of the mechanical mode could be reduced *in situ* by up to about 50% via mass enhancement from the fluid without adding extra dissipation. We find that the damping rate due to TTLS scales approximately as $\Delta f_{\text{TTLS}} \propto f_0$, while scaling $\Delta f_{\text{TTLS}} \propto 1/m \propto f_0^2$ is expected from mass loading only. Thus, intrinsic drag due to TTLS is increased in the fluid. We attribute the increased damping to a TTLS phonon coupling parameter γ_1 taken at the device frequency f_0, and scaling approximately as $\gamma_1 \propto f_0^{-1/2}$. In future, systematic studies on

the parameter γ_1 as a function of device frequency could be done by measurements at various fluid densities, which allows further tuning of the frequency of the devices by up to 7%.

Another important damping mechanism in our devices is magnetomotive damping. We find that magnetomotive damping is independent of frequency in the frequency range 30 to 400 kHz, and the corresponding damping rate is inversely proportional to the effective mass of the resonator. In addition, changing the frequency allowed us to study the previously unidentified temperature-independent damping mechanism in our devices [5], and we propose overdamped oscillations of the carrier chip as a possible explanation for the observed damping.

In our devices, large frequency tuning by mass loading from fluid is achieved by making devices with large aspect ratio, where the ratio of beam width to thickness is ~100 in wider devices. As mechanical resonators are the most sensitive to forces acting on the device at the mechanical resonance frequency, the frequency tuning has many potential applications in studying effects that occur at specific frequencies. Examples of such effects are resonant Kelvin waves on quantized vortices in superfluids [36,37], acoustic modes in cavities [38], and vortex-core bound states in superfluid ^{3}He [4]. Beyond superfluids, the frequency tuning could be utilized, for instance, in NEMS based nuclear magnetic resonance measurements [2].

At $T > 0.2$ K contributions from thermal excitations of ^{4}He, namely, phonons and rotons, increase the damping of the NEMS devices. Good agreement with existing theory is found, but with some differences in the scattering efficiencies found between the devices, perhaps due to proximity to surfaces and different aspect ratios. The devices are very sensitive to the quasiparticles due to the large surface area and small mass, and the calibrated devices could be used for precise thermometry in superfluid ^{4}He. As the temperature is increased further, above $T > 0.8$ K, viscous effects become important. The obtained geometrical parameters are close to unity, as expected, and agreement between different devices is good. The same geometrical parameters work in the normal and superfluid states of ^{4}He. This shows that similar devices could be used for viscometry, and thermometry in superfluid ^{4}He, with good precision without free parameters.

APPENDIX A: TTLS SATURATION TEMPERATURE T^* IN DIFFERENT DIMENSIONS

The spatially and orientationally averaged TTLS relaxation rate is [5,6]

$$\langle \tau_1^{-1}(\epsilon) \rangle_V = \frac{1}{V} g(\epsilon) \frac{\Delta_0^2}{\epsilon} \frac{\pi \gamma^2}{E \hbar^2} \coth\left(\frac{\epsilon}{2k_B T}\right), \qquad (A1)$$

where $g(\epsilon)$ is the phonon density of states, and $\epsilon = \sqrt{\Delta_0^2 + \Delta^2}$ is the TTLS energy, Δ_0 is the tunneling strength, and Δ is the double-well asymmetry. The densities of states for flexural phonons in 1D and 2D are given by $g_{1D}(\epsilon) \propto \epsilon^{-1/2}$ and $g_{2D}(\epsilon) \propto \epsilon^0$, respectively [5,6], and for bulk phonons $g_{3D}(\epsilon) = \epsilon^2$ [29]. The minimum relaxation time $\tau_{1,\min}$ is obtained for the TTLS states with $\epsilon = \Delta_0$. Inserting the density of states in Eq. (A1), we get

$$\tau_{1,\min,1D} \propto \epsilon^{-1/2} \coth^{-1}\left(\frac{\epsilon}{2k_B T}\right) \propto \epsilon^{1/2}|_{\epsilon \ll k_B T},$$

$$\tau_{1,\min,2D} \propto \epsilon^{-1} \coth^{-1}\left(\frac{\epsilon}{2k_B T}\right) \propto \epsilon^0|_{\epsilon \ll k_B T}, \qquad (A2)$$

$$\tau_{1,\min,3D} \propto \epsilon^{-3} \coth^{-1}\left(\frac{\epsilon}{2k_B T}\right) \propto \epsilon^{-2}|_{\epsilon \ll k_B T},$$

where only the states up to $\epsilon \approx k_B T$ are relevant [5]. For the states with $\epsilon = k_B T$, we have

$$\tau_{1,\min,1D}(\epsilon = k_B T) \propto (k_B T)^{-1/2},$$

$$\tau_{1,\min,2D}(\epsilon = k_B T) \propto (k_B T)^{-1}, \qquad (A3)$$

$$\tau_{1,\min3D}(\epsilon = k_B T) \propto (k_B T)^{-3}.$$

We require that

$$2\pi f_0 \tau_{1,\min}(\epsilon = k_B T^*) = 1,$$

which results in

$$T_{1D}^* \propto f_0^2,$$

$$T_{2D}^* \propto f_0,$$

$$T_{3D}^* \propto f_0^{1/3}. \qquad (A4)$$

The expressions are useful when comparing changes in T^* within devices of the same dimensionality, but some caution is advised if the same are to be applied to devices of different dimensionalities. It follows from the right-hand-side terms in Eq. (A2) that in 1D, $\tau_{1,\min,1D}(\epsilon = k_B T_{1D}^*)$ is a maximum, i.e., the TTLS with $\epsilon < k_B T$ have shorter relaxation times. Thus, T_{1D}^* marks the temperature above which practically all TTLS have $2\pi f_0 \tau_1 \lesssim 1$. Similarly, it follows that in 2D $\tau_{1,\min,2D}(\epsilon)$ is almost independent of the energy and T_{2D}^* marks the temperature where practically all TTLS have $2\pi f_0 \tau_1 \sim 1$. In 3D, $\tau_{1,\min,3D}(\epsilon = k_B T_{3D}^*)$ is a minimum, i.e., the TTLS with $\epsilon < k_B T$ have longer relaxation times and mark the temperature below which practically all TTLS have $2\pi f_0 \tau_1 \gtrsim 1$.

APPENDIX B: ADDED MASS CONTRIBUTION TO PHONON DISPERSION RELATION

Analytical expressions for TTLS damping in reduced dimensions usually rely on expressions derived from phonon dispersion relation for a simple geometry, such as a beam or plate in vacuum [5,6,9]. Here, we extend these models from the simplest case of a beam in vacuum to a beam in fluid, taking into account change in the phonon dispersion relation due to increase in the effective mass.

The dispersion relation for flexural phonons in a rectangular cantilever beam is given by

$$\omega = k_{ph}^2 \sqrt{\frac{E I_x}{\rho_{Al} w d}}, \qquad (B1)$$

where k_{ph} is the phonon wave number, E is the Young's modulus, $I_x = w d^3 / 12$ is the second moment of inertia, w is the beam width, and d is the thickness. Strictly speaking, Eq. (B1) is valid only in vacuum, and in fluid it should be modified by the presence of the fluid via mass loading.

The flexural phonon frequencies given by Eq. (B1) are closely related to the natural frequencies of a fixed-free cantilever beam. For a beam of length H, width w, and thickness d, the natural frequencies are given by [39]

$$\omega_0 = \frac{k_n}{H^2} \sqrt{\frac{E I_x}{\rho_{Al} w d}}, \qquad (B2)$$

where k_n are the roots of the equation $\cos(\sqrt{k_n}) \cosh(\sqrt{k_n}) + 1 = 0$, where n is the mode number. For example, for the first three modes $k_1 \approx 3.52$, $k_2 \approx 22.0$, and $k_3 \approx 61.7$. The free end of the beam is an antinode, and consequently the eigenmodes are odd multiples of the quarter wavelength of the corresponding flexural phonons. This is seen by setting $k_{ph} = (2n-1)\pi/(2H)$ in Eq. (B1), which produces values close to that of Eq. (B2), with decreasing deviation as the mode number n increases.

When a device is immersed in a fluid, its effective mass increases, and its resonance frequency decreases according to Eq. (1). Our experiments show that the mass enhancement at low temperatures results solely from the potential flow of the fluid [first term in Eq. (9), on the right-hand side]. The parameter β describing the potential flow is by first principles obtained by integrating the fluid velocity field around the device [35]. Due to the close resemblance between flexural phonon modes and the mechanical eigenmodes of the device, we believe that flexural phonons with sufficiently low frequencies should scale similarly as the mechanical mode, when immersed in the fluid

$$\omega_{LHe} = \left(\frac{\omega_{0,LHe}}{\omega_{0,vac}}\right) \omega. \qquad (B3)$$

In terms of the parameters appearing in Eqs. (13), (14), (B1), and (B2), the change in the frequency can be conveniently incorporated in an effective speed of sound $c_{LHe} = (\omega_{0,LHe}/\omega_{0,vac})c$.

At sufficiently high frequencies, the velocity along the beam varies at a length scale which is shorter than the beam width, which sets the relevant hydrodynamic length scale [28]. In this case, fluid can take a shortcut by moving from antinode to antinode, rather than around the beam. With increasing frequency the distance between antinodes decreases, and we expect that the mass enhancement from the potential flow diminishes. For the wide devices W1 and W2, the flexural

phonon wavelength becomes smaller than the beam width at around 5 MHz, and for the narrow devices N1 and N2 at around 1 GHz. At higher phonon frequencies, the vacuum phonon dispersion relation given by Eq. (B1) is expected to hold.

Equations (13) and (14), describing TTLS losses in 1D and 2D devices, respectively, are derived from an integral of the form [6]

$$\Delta f \propto \frac{1}{k_B T} \int_0^\infty d\epsilon \left[\epsilon g(\epsilon) \mathrm{csch}\left(\frac{\epsilon}{k_B T} \right) \right], \qquad \text{(B4)}$$

where ϵ is the TTLS energy, and $g(\epsilon)$ is the phonon density of states introduced in Appendix A. The $\mathrm{csch}(\epsilon/k_B T)$ term imposes a temperature-dependent cutoff frequency. For the wide 2D devices W1 and W2, the dominant contribution to this integral at $T > 1\,\mathrm{mK}$ comes from phonons with frequency above 5 MHz. Thus, we expect that mass enhancement in fluid is irrelevant for the expression given in Eq. (14). For the narrow 1D devices N1 and N2, a substantial fraction to the integral is contributed by phonon states below 1 GHz, and they give the dominant contribution to the integral at $T < 0.2\,\mathrm{K}$. The relative importance of the mass-scaled phonon frequencies decreases with increasing temperature due to the temperature-dependent cutoff frequency. The maximum relative error in damping resulting from using the vacuum speed of sound in Eq. (13) for the device N1 is

$$1 - \sqrt{c/c_\mathrm{LHe}} = 1 - \sqrt{f_{0,\mathrm{vac}}/f_{0,\mathrm{LHe}}} \approx -8\%.$$

The expected effect for the narrow device N1 is on par with other error sources.

[1] M. Li, Ultra-sensitive NEMS-based cantilevers for sensing, scanned probe and very high-frequency applications, Nat. Nanotechnol. **2**, 114 (2007).

[2] C. Müller, Nuclear magnetic resonance spectroscopy with single spin sensitivity, Nat. Commun. **5**, 4703 (2014).

[3] A. Guthrie, Nanoscale real-time detection of quantum vortices at millikelvin temperatures, Nat. Commun. **12**, 2645 (2021).

[4] N. B. Kopnin and M. M. Salomaa, Mutual friction in superfluid ³He: Effects of bound states in the vortex core, Phys. Rev. B **44**, 9667 (1991).

[5] T. Kamppinen, J. T. Mäkinen, and V. B. Eltsov, Dimensional control of tunneling two-level systems in nanoelectromechanical resonators, Phys. Rev. B **105**, 035409 (2022).

[6] R. O. Behunin, F. Intravaia, and P. T. Rakich, Dimensional transformation of defect-induced noise, dissipation, and nonlinearity, Phys. Rev. B **93**, 224110 (2016).

[7] G. Ithier, E. Collin, P. Joyez, P. J. Meeson, D. Vion, D. Esteve, F. Chiarello, A. Shnirman, Y. Makhlin, J. Schriefl, and G. Schön, Decoherence in a superconducting quantum bit circuit, Phys. Rev. B **72**, 134519 (2005).

[8] L. M. de Lépinay, C. F. Ockeloen-Korppi, M. J. Woolley, and M. A. Sillanpää, Quantum mechanics-free subsystem with mechanical oscillators, Science **372**, 625 (2021).

[9] C. Seoánez, F. Guinea, and A. H. Castro Neto, Surface dissipation in nanoelectromechanical systems: Unified description with the standard tunneling model and effects of metallic electrodes, Phys. Rev. B **77**, 125107 (2008).

[10] R. Blaauwgeers, M. Blazkova, M. Človečko, V. B. Eltsov, R. de Graaf, J. Hosio, M. Krusius, D. Schmoranzer, W. Schoepe, L. Skrbek, P. Skyba, R. E. Solntsev, and D. E. Zmeev, Quartz tuning fork: Thermometer, pressure- and viscometer for helium liquids, J. Low Temp. Phys. **146**, 537 (2007).

[11] D. I. Bradley, P. Crookston, S. N. Fisher, A. Ganshin, A. M. Guénault, R. P. Haley, M. J. Jackson, G. R. Pickett, R. Schanen, and V. Tsepelin, The damping of a quartz tuning fork in superfluid ³He-B at low temperatures, J. Low Temp. Phys. **157**, 476 (2009).

[12] H. Yano, A. Handa, H. Nakagawa, K. Obara, O. Ishikawa, T. Hata, and M. Nakagawa, Observation of laminar and turbulent flow in superfluid ⁴He using a vibrating wire, J. Low Temp. Phys. **138**, 561 (2005).

[13] V. B. Efimov, D. Garg, M. Giltrow, P. V. E. McClintock, L. Skrbek, and W. F. Vinen, Experiments on a high quality grid oscillating in superfluid ⁴He at very low temperatures, J. Low Temp. Phys. **158**, 462 (2010).

[14] J. Jäger, B. Schuderer, and W. Schoepe, Translational oscillations of a microsphere in superfluid helium, Phys. B: Condens. Matter **210**, 201 (1995).

[15] M. Defoort, S. Dufresnes, S. L. Ahlstrom, D. I. Bradley, R. P. Haley, A. M. Guénault, E. A. Guise, G. R. Pickett, M. Poole, A. J. Woods, V. Tsepelin, S. N. Fisher, H. Godfrin, and E. Collin, Probing Bogoliubov quasiparticles in superfluid ³He with a 'vibrating-wire like' MEMS device, J. Low Temp. Phys. **183**, 284 (2016).

[16] A. M. Guénault, A. Guthrie, R. P. Haley, S. Kafanov, Y. A. Pashkin, G. R. Pickett, M. Poole, R. Schanen, V. Tsepelin, D. E. Zmeev, E. Collin, O. Maillet, and R. Gazizulin, Probing superfluid ⁴He with high-frequency nanomechanical resonators down to millikelvin temperatures, Phys. Rev. B **100**, 020506(R) (2019).

[17] P. Zheng, W. G. Jiang, C. S. Barquist, Y. Lee, and H. B. Chan, Anomalous Damping of a Microelectromechanical Oscillator in Superfluid ³He-B, Phys. Rev. Lett. **117**, 195301 (2016).

[18] T. Kamppinen and V. B. Eltsov, Nanomechanical resonators for cryogenic research, J. Low Temp. Phys. **196**, 283 (2019).

[19] E. Collin, Y. M. Bunkov, and H. Godfrin, Addressing geometric nonlinearities with cantilever microelectromechanical systems: Beyond the Duffing model, Phys. Rev. B **82**, 235416 (2010).

[20] A. Cleland and M. Roukes, External control of dissipation in a nanometer-scale radiofrequency mechanical resonator, Sens. Actuators, A **72**, 256 (1999).

[21] W. F. Vinen and L. Skrbek, Quantum turbulence generated by oscillating structures, Proc. Natl. Acad. Sci. USA **111**, 4699 (2014).

[22] M. J. Fear, P. M. Walmsley, D. E. Zmeev, J. T. Mäkinen, and A. I. Golov, No effect of steady rotation on solid ⁴He in a torsional oscillator, J. Low Temp. Phys. **183**, 106 (2016).

[23] B. M. Abraham, Y. Eckstein, J. B. Ketterson, M. Kuchnir, and P. R. Roach, Velocity of sound, density, and grüneisen constant in liquid ⁴He, Phys. Rev. A **1**, 250 (1970).

[24] R. J. Donnelly and C. F. Barenghi, The observed properties of liquid helium at the saturated vapor pressure, J. Phys. Chem. Ref. Data **27**, 1217 (1998).

[25] H. Godfrin, K. Beauvois, A. Sultan, E. Krotscheck, J. Dawidowski, B. Fåk, and J. Ollivier, Dispersion relation of Landau elementary excitations and thermodynamic properties of superfluid ^{4}He, Phys. Rev. B **103**, 104516 (2021).

[26] J. S. Brooks and R. J. Donnelly, The calculated thermodynamic properties of superfluid helium-4, J. Phys. Chem. Ref. Data **6**, 51 (1977).

[27] R. D. Mc Carty, Thermodynamic properties of helium 4 from 2 to 1500 K at pressures to 10^8 Pa, J. Phys. Chem. Ref. Data **2**, 923 (1973).

[28] J. E. Sader, Frequency response of cantilever beams immersed in viscous fluids with applications to the atomic force microscope, J. Appl. Phys. **84**, 64 (1998).

[29] W. A. Phillips, Two-level states in glasses, Rep. Prog. Phys. **50**, 1657 (1987).

[30] G. Baym, R. G. Barrera, and C. J. Pethick, Mobility of the Electron Bubble in Superfluid Helium, Phys. Rev. Lett. **22**, 20 (1969).

[31] M. Niemetz and W. Schoepe, Stability of laminar and turbulent flow of superfluid ^{4}He at mK temperatures around

[32] G. W. Rayfield and F. Reif, Quantized vortex rings in superfluid helium, Phys. Rev. **136**, A1194 (1964).

[33] S. Yorozu, H. Fukuyama, and H. Ishimoto, Isochoric pressure and ^{3}He quasiparticle effective mass in a ^{3}He $-^4$He mixture under pressure, Phys. Rev. B **48**, 9660 (1993).

[34] H. Wakita and Y. Sano, ^{3}He/^{4}He ratios in CH_4-rich natural gases suggest magmatic origin, Nature (London) **305**, 792 (1983).

[35] L. D. Landau and E. M. Lifshitz, *Fluid Mechanics*, 2nd ed. (Butterworth-Heineman, Oxford, 1987).

[36] W. F. Vinen, M. Tsubota, and A. Mitani, Kelvin-Wave Cascade on a Vortex in Superfluid ^{4}He at a Very Low Temperature, Phys. Rev. Lett. **91**, 135301 (2003).

[37] V. B. Eltsov and V. S. L'vov, Amplitude of waves in the Kelvin-wave cascade, JETP Lett. **111**, 389 (2020).

[38] A. B. Shkarin, A. D. Kashkanova, C. D. Brown, S. Garcia, K. Ott, J. Reichel, and J. G. E. Harris, Quantum Optomechanics in a Liquid, Phys. Rev. Lett. **122**, 153601 (2019).

[39] L. D. Landau, E. M. Lifshitz, A. M. Kosevich, L. P. Pitaevskii, J. B. Sykes, and W. H. Reid, *Landau and Lifshitz Course of Theoretical Physics, Theory of Elasticity*, 3rd ed., Vol. 7 (Elsevier, Amsterdam, 1986).